Future changes in stratospheric quasi-stationary wave-1 in the extratropical southern hemisphere spring and summer as simulated by ACCESS-CCM

Kane A. Stone [iD] [A,B,C,E], *Andrew R. Klekociuk* [iD] [A,D] *and Robyn Schofield* [iD] [A,B]

[A] School of Geography, Earth, and Atmospheric Sciences, University of Melbourne, Melbourne, Australia.
[B] ARC Centre of Excellence for Climate System Science, Sydney, Australia.
[C] Present address: The Department of Earth, Atmospheric and Planetary Sciences, Massachusetts Institute of Technology, Cambridge, Massachusetts 02139-4307, USA.
[D] Australian Antarctic Division, Hobart, Australia.
[E] Corresponding author. Email: stonek@mit.edu

Abstract. Seasonally dependent quasi-stationary planetary wave activity in the southern hemisphere influences the distribution of ozone within and near the equatorward edge of the stratospheric polar vortex. Accurate representation of this zonal asymmetry in ozone is important in the characterisation of stratospheric circulation and climate and their associated effects at the surface. In this study, we used the Australian Community and Climate Earth System Simulator-Chemistry Climate Model to investigate the influence of greenhouse gases (GHGs) and ozone depleting substances (ODSs) on the zonal asymmetry of total column ozone (TCO) and 10 hPa zonal wind between 50 and 70°S. Sensitivity simulations were used from 1960 to 2100 with fixed ODSs and GHGs at 1960 levels and a regression model that uses equivalent effective stratospheric chlorine and carbon dioxide equivalent radiative forcing as the regressors. The model simulates the spring and summer zonal wave-1 reasonably well, albeit with a slight bias in the phase and amplitude compared to observations. An eastward shift in the TCO and 10 hPa zonal wave-1 is associated with both decreasing ozone and increasing GHGs. Amplitude increases are associated with ozone decline and amplitude decreases with GHG increases. The influence of ODSs typically outweigh those by GHGs, partly due to the GHG influence on TCO phase at 50°S likely being hampered by the Andes. Therefore, over the 21st century, influence from ozone recovery causes a westward shift and a decrease in amplitude. An exception is at 70°S during spring, where the GHG influence is larger than that of ozone recovery, causing a continued eastward trend throughout the 21st century. Also, GHGs have the largest influence on the 10 hPa zonal wave-1 phase, but still only induce a small change in the wave-1 amplitude. Different local longitudes also experience different rates of ozone recovery due to the changes in phase of the zonal wave-1. The results from this study have important implications for understanding future ozone layer distribution in the Southern Hemisphere under changing GHG and ODS concentrations. Important future work would involve conducting a similar study using a large ensemble of models to gain more statistically significant results.

Keywords: ACCESS-CCM, climate, climate modelling, greenhouse gases, Multi Sensor Reanalysis, ozone depletion, ozone layer, quasi-stationary planetary wave, southern hemisphere, stratospheric circulation.

1 Introduction

Planetary (Rossby) waves play an important role in setting the general thermal and dynamical characteristics of the troposphere and stratosphere at extratropical and polar latitudes. These waves arise as a consequence of conservation of potential vorticity and the latitudinal gradient of the Coriolis force and are generated primarily in the troposphere through deep convection associated with land–sea temperature contrasts and dynamical forcing associated with continental-scale orographic features (Charney and Drazin 1961; Kurzeja 1984; Karoly and Vincent 1998; Brasseur and Solomon 2005). Charney and Drazin (1961) showed that the upward propagation of quasi-stationary Rossby waves (QSWs), that is, those waves that remain relatively fixed in longitude over periods that characteristically range from weeks to

months, requires background eastward wind speeds less than a critical value. This critical value is dependent on zonal wavenumber and generally results in only waves of wavenumber 1–3 being able to propagate from the troposphere into the stratosphere (Brasseur and Solomon 2005) and only under appropriate conditions for wavenumber 3 (Rao *et al.* 2019).

The observed characteristics of QSWs in the southern hemisphere (SH) have been well-studied through the use of meteorological reanalyses and satellite measurements to examine zonal perturbations in atmospheric variables, such as geopotential height and temperature (van Loon and Jenne 1972; Hartmann 1977; Karoly 1985; Randel 1988; Quintanar and Mechos 1995), ozone (Wirth 1993; Gabriel *et al.* 2011; Wang *et al.* 2013; Dennison *et al.* 2017) and water vapour (Gabriel *et al.* 2011). In general, it has been found (e.g. Randel 1988) that the QSW wave variance in the SH stratosphere peaks in October in the latitude band 50–60°S, with a secondary maximum in May. In the SH troposphere, relative maxima in the wave variance are found in late winter and early spring in the latitude bands 30–40°S and 50–60°S respectively (Randel 1988). Regional contrasts in tropical sea surface temperatures (SSTs) provide an important source of forcing for the QSWs at extratropical latitudes, particularly over the Indian and Pacific oceans (Quintanar and Mechos 1995; Brahmananda Rao *et al.* 2004; Inatsu and Hoskins 2004). It has also been shown that there is destruction interference in the forcings from the tropical Pacific Ocean and the tropical Indian Ocean on the winter SH stratosphere (Rao and Ren 2020).

QSWs in the troposphere and lower stratosphere of the extratropical SH have important influences on the total column ozone (TCO) distribution in the region (Wirth 1993; Gabriel *et al.* 2011; Wang *et al.* 2013). The waves influence the poleward transport of air in the lower stratosphere by driving the poleward branch of the Brewer-Dobson circulation. This in turn influences the background thermal state and chemical composition of the lower stratosphere, and hence, ozone production and loss. Additionally, the waves play a role in setting the height of the tropopause, which in turn determines the effective thickness of the stratosphere, and hence, the column abundance of ozone (Varotsos *et al.* 2004; Gerber 2012). During spring, marked zonal asymmetries in tropopause height are produced by the strong radiative influences associated with depletion of ozone within the Antarctic ozone hole and the influence of QSWs on the ozone distribution outside the stratospheric polar vortex (Evtushevsky *et al.* 2008). In contrast, zonal asymmetries in tropopause height during summer are mainly influenced by surface temperature contrasts and the associated synoptic-scale tropospheric patterns that are produced by travelling Rossby waves (Hoinka 1998).

During the satellite era since 1979, in which TCO measurements have achieved consistent global coverage, the extratropical QSW-1 pattern in TCO has shown long-term changes. Grytsai *et al.* (2007*a*) examined historical trends in the phase of QSW-1 in spring (averaging over September–November) by analysing the change in the longitudes of the minimum and maximum TCO (TCO_{min} and TCO_{max} respectively) values as a function of latitude and year. A clear eastward trend was found in the longitude of the zonal TCO_{min}, consistent with that reported by Niu *et al.* (1992), but little trend was seen in the location of the zonal TCO_{max}. Furthermore, strong latitude dependence was shown on the phase of the QSW-1 component, with increased eastward shift at higher latitudes. Ialongo *et al.* (2012) characterised the springtime ozone zonal waves and showed that the QSW-1 pattern was dominant and detectable up to altitudes of 60–65 km and that an eastward travelling wave-2 was also present.

The response of stationary waves in the SH to different long-term drivers, such as changes in ozone and well-mixed greenhouse gasses (GHGs) has been investigated previously in a model-based study (Wang *et al.* 2013). It was shown that stratospheric ozone change was the main driver of changes in QSW amplitude; however this had little influence on the eastward phase change seen in QSW-1. Instead, this work noted that phase trends are associated mostly with GHG changes influencing the strength of the subtropical tropospheric jet. Wang *et al.* (2013) concluded that future long-term dynamical changes in the structure of QSWs are expected to be driven by changing springtime Antarctic GHG and stratospheric ozone concentrations, which are both responsible for changes in the polar vortex, the tropospheric westerly jets and tropospheric wave sources.

The primary focus of this paper is the investigation of the future drivers of TCO QSWs using the Australian Community Climate and Earth System Simulator-Chemistry Climate Model (ACCESS-CCM) following Stone (2015). Firstly, formation of TCO QSWs within ACCESS-CCM and how they compare to observations will be discussed for austral spring (September–November) and summer (December–February), as these time periods display the largest Antarctic ozone depletion and strongest stratosphere–troposphere coupling. This is followed by attribution of past and future changes in the phase and amplitude of TCO and 10 hPa zonal wind through a multiple linear regression model. Finally, aspects of localised impacts on ozone depletion and recovery are discussed, relating to longitudinal deviations in ozone change over time and how this could potentially affect shortwave radiation fluxes at the surface.

2 Data and methods

2.1 ACCESS-CCM

A description of the ACCESS-CCM model and its performance in simulating ozone in the SH is provided in detail in Stone *et al.* (2016) and Morgenstern *et al.* (2017). The model is similar to the National Institute of Water and Atmospheric Research (NIWA) chemistry climate model (NIWA-UKCA) (Morgenstern *et al.* 2009, 2014, 2017), which is based on the United Kingdom Chemistry and Aerosols (UKCA) of the United Kingdom Meteorological Office. The simulations used in this study were produced for the Phase 1 of the Chemistry-Climate Model Initiative (Eyring *et al.* 2013*b*). The simulations used here are a hindcast simulation over 1960–2010, labelled REF-C1, a projection simulation over 1960–2100, labelled REF-C2, and two sensitivity simulations over 1960–2100 with (separately) fixed ozone depleting substances (ODSs) and GHGs at 1960 levels, labelled SEN-C2-fODS and SEN-C2-fGHG respectively (Eyring *et al.* 2013*b*). As ACCESS-CCM does not have an interactive ocean, SSTs and sea ice concentrations (SICs) are
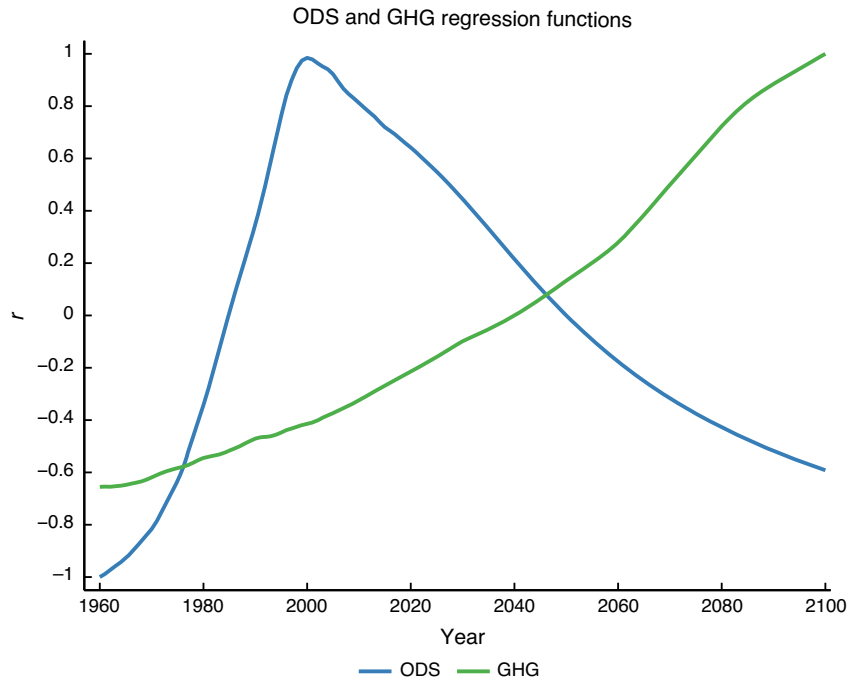
Fig. 1. ODS and GHG regression functions. Both functions are normalised to have an average of 0 and absolute maximum of 1.

prescribed values, sourced from the Hadley Centre Sea Ice and Sea Surface Temperature dataset for the REF-C1 simulation (Rayner *et al.* 2003), and from the Hadley Centre Global Environment Model version 2 ensemble run r1p1i1 from the fifth Coupled Model Intercomparison Project (CMIP5) for the REF-C2, SEN-C2-fODS and SEN-C2-fGHG simulations. For the SEN-C2-fGHG simulation, the SSTs and SICs were repeated 1960–1970 levels to avoid a SST induced GHG signal. The REF-C1 simulation used observed GHG and ODS data from Meinshausen *et al.* (2011) and WMO (2011) respectively. After 2005, GHGs followed the Representative Concentration Pathway 8.5 (RCP 8.5). For the historical period of 1960–2000, the projection simulations used the same forcings as the REF-C1 simulation. After 2000, RCP 6.0 was used for GHGs, and the A1B emissions scenario from WMO (2011) was used. Model runs were initiated from a control simulation. The model was run at an N48 (3.75° longitude by 2.5° latitude) horizontal resolution and L60 (60 hybrid height levels) vertical resolution with a model top of 84 km.

2.2 Multi Sensor Reanalysis (MSR)

For comparison with our model results, we used the MSR dataset version 2 (Van Der A *et al.* 2015). MSR is based on near-ultraviolet TCO measurements using polar orbiting satellites. The observations were corrected using ground-based measurements and synthesised into monthly averages of TCO on a global grid (1.0° longitude × 1.0° latitude in MSR version 2) using a data assimilation scheme that is based on a chemical transport model driven by a meteorological reanalysis. We used MSR data from 1979 to 2014.

2.3 Regression model

We separated and quantified the influence of GHGs and ODSs, the two long-term SH drivers of stratospheric and tropospheric circulation and dynamics, through the use of a linear regression model. Our regression model is similar to that adopted by Morgenstern *et al.* (2014) and has two predictors: (1) Effective Equivalent Stratospheric Chlorine (EESC) obtained from WMO (2011) and (2) carbon dioxide equivalent radiative forcing (CO_2eq) from well-mixed GHGs following the RCP 6.0 scenario (Meinshausen *et al.* 2011). The EESC calculation used an age of air value for the polar regions of 5.5 years, consistent with Newman *et al.* (2007). These two predictors acted as regression functions in our model. They both covered the period from 1960 to 2100 and were normalised to span the range –1 to 1 with the mean equal to 0 to make them easier to visually compare how they change over time. It is important to note that when using multivariate regression, any non-linear interaction will not be captured. These functions are shown in Fig. 1. The EESC regression function was set to 0 for the SEN-C2-fODS experiment, as we have normalised the regression functions to have a mean of zero and ozone in this simulation is not influenced by ODS; likewise, the CO_2eq regression function was set to zero for the SEN-C2-fGHG experiment. To simplify the notation in our approach, the CO_2eq and EESC regression functions are hereafter subscripted with GHG and ODS, respectively, to denote their drivers. The model is defined as:

$$y = \beta_{ODS}x_{ODS} + \beta_{GHG}x_{GHG} + \bar{y} + \varepsilon \qquad (1)$$

where y is the time series being regressed against at a particular time, β_{ODS} is the regression coefficient related to the ODS

regression function, x_{ODS}, which quantifies the influence of ozone depletion with respect to a unit change in ODS, β_{GHG} is the regression coefficient describing the influence of a unit change in the GHG regression function, x_{GHG}, $\bar{y}$ is the mean of the time series over the time period under consideration, and ε is a residual term which accounts for contributions not described by the regression functions. The fit of the model was performed using the method of least squares, and uncertainties were obtained for β_{ODS} and β_{GHG} at the 95% confidence intervals using a regression model F-test. We described the influence from the ODS and GHG regression functions over the periods of ODS growth (1960–2000) and decline (2001–2100) by multiplying the regression coefficients with their associated regression function changes over the respective two periods.

To characterise QSW-1, we separately used for y in the regression model the amplitude (A_1) and phase (Φ_1) of the first harmonic in the Fourier decomposition of zonal TCO at each discrete latitude in ACCESS-CCM. The Fourier decomposition is described by equation 1 of Ialongo *et al.* (2012), and we obtained the wave-1 coefficients of the decomposition, a_1 and b_1, from a discrete Fourier transform of the zonal TCO, 10 hPa zonal wind and 500 hPa zonal temperature. The wave-1 amplitude and phase were evaluated as $A_1 = \sqrt{a_1^2 + b_1^2}$ and $\Phi_1 = \tan^{-1}\left(\frac{b_1}{a_1}\right)$ respectively.

3 ACCESS-CCM representation of zonal waves

Fig. 2 shows the 1979–2010 TCO spring and summer average zonal TCO variation at 50°S latitude for both the REF-C2 simulation and the MSR dataset. It is apparent in this figure that the ACCESS-CCM simulates excess ozone concentrations compared to observations (approximately 5–40 Dobson Units (DU) depending on longitude and season, or approximately less than 15% relative to the mean). However, the ACCESS-CCM zonal wave structure in both spring and summer is similar to MSR. During spring, a wave-1 pattern dominates with the average REF-C2 wave-1 amplitude being 17.5 DU compared to 3.1 DU for wave-3, and average MSR wave-1 amplitude being 24.7 DU compared to 3.3 DU for wave-3. During summer, both distinct wave-1 and wave-3 patterns are present, with the average REF-C2 wave-1 amplitude being 8.0 DU compared to 2.7 DU for wave-3, and average MSR wave-1 amplitude being 9.2 DU compared to 4.0 DU for wave-3. There is a relatively small difference in the phase of the overall patterns between the two data sets, with the REF-C2 pattern shifting approximately 25° westward during spring compared with the observations (Fig. 2a). Additionally, both REF-C2 and REF-C1 have very similar structure over this time period (not shown). The peak-to-trough amplitude of the wave-1 in REF-C2 is somewhat smaller, although it is generally consistent with MSR in spring. However, at higher latitudes in spring, REF-C2 has a noticeably smaller wave-1 amplitude compared to MSR (not shown). Smaller wave amplitudes compared to reanalysis have also been reported in other models. For example, Covey *et al.* (2020) reported smaller wave-1 and wave-3 amplitudes in the northern hemisphere and also smaller wave-3 amplitudes in the SH in the Community Earth System Model 2, Geophysical Fluid Dynamics Laboratory-Climate
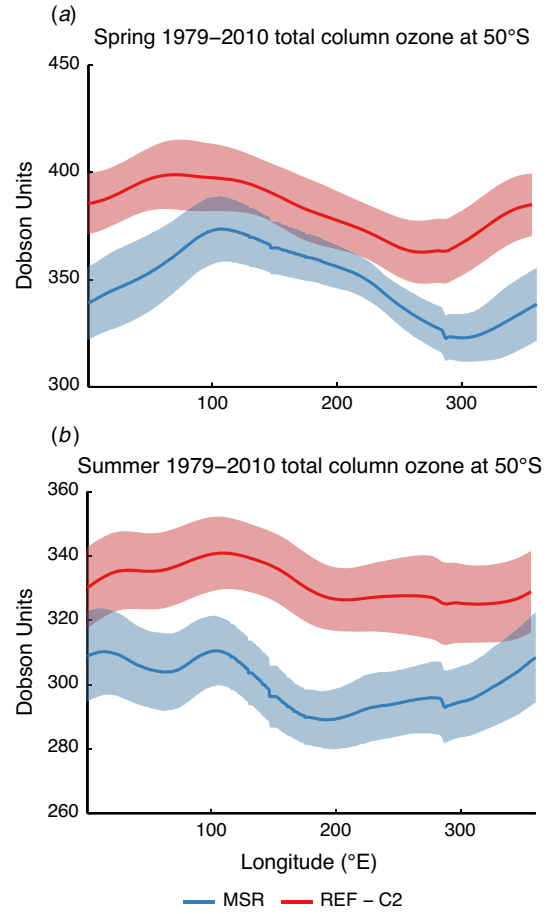

Fig. 2. (*a*) Spring and (*b*) summer 50°S TCO averaged over the 1979–2010 period as simulated by the REF-C2 simulation compared to observations from the MSR dataset. The shaded region encompasses one standard deviation.

Model 4 and Goddard Institute for Space Studies-E2-1-G model. In the spring MSR data, the wave-1 component is largest compared to other the wave components at 65°S. This is generally seen in the REF-C2 simulation, with latitudes of 60 and 65°S having a dominant wave-1 component. During summer, the wave-1 component is largest compared to wave-2 and wave-3 near 60°S in MSR. However, in REF-C2, this occurs at 70°S, which is most likely due to the differing times of the break-up of the polar vortex in the model compared to observations (Stone 2015; Stone *et al.* 2016).

The MSR profiles of Fig. 2 show small downward perturbations at longitudes of approximately 150 and 290°E (70°W), which geographically correspond to the southern tip of New Zealand and the Andes at this latitude respectively. These features are sharper in the observations than the model (and largely absent in the model data at 150° longitude), which is likely due to the different spatial resolutions of the data sets ($1.0° \times 1.0°$ in longitude and latitude for MSR compared with $3.75° \times 2.5°$ for ACCESS-CCM) and the relatively coarse resolution of the topography used in the model. Notably, these features suggest that the underlying topography potentially lifts

Table 1.   Square of the Pearson linear correlation coefficient between 500 hPa temperature (T500) and lapse-rate tropopause height (LRTH), and LRTH and total column ozone (TCO) for meridional averages between 45 and 65°S as a function of season over 1979–2010 from the REF-C2 run of ACCESS-CCM and ERA-Interim

Values in bold are significant at the 95% confidence limit based on Student's *t*-test. Before averaging, the ERA-Interim data were re-gridded to the same spatial resolution as the ACCESS-CCM data. SON, September, October, November; DJF, December, January, February; MAM, March, April, May; JJA, June, July, August

Season	ACCESS-CCM		ERA-Interim	
	T500 vs LRTH	LRTH vs TCO	T500 vs LRTH	LRTH vs TCO
Spring (SON)	**0.53**	**0.82**	0.03	**0.98**
Summer (DJF)	**0.70**	0.13	**0.96**	**0.74**
Autumn (MAM)	**0.72**	0.30	**0.93**	0.25
Winter (JJA)	**0.67**	0.62	0.18	0.39

the tropopause in these regions through the action of orographic waves, which would be expected to displace stratospheric air horizontally above these regions, and thus, locally reduce the ozone overburden. Therefore, it can be expected that the broader longitudinal variations shown in Fig. 2 may be influenced by the height of the tropopause. We investigated this aspect by examining the zonal variations of TCO, tropopause height and the temperature of the midtroposphere. For this, we obtained the latitudinal-average zonal profiles of TCO, tropopause height and 500 hPa air temperature for each season from the REF-C2 simulation over 1979–2010. For comparison, equivalent observationally based information was obtained over the same time period from the European Centre for Medium-Range Weather Forecasts Interim Reanalysis (ERA-Interim; Dee *et al.* 2011). The location of the lapse-rate tropopause was used to define the height of the tropopause, and this was evaluated using the method described by Reichler *et al.* (2003). Table 1 summarises seasonal differences in the extratropical coupling between the troposphere and tropopause and the tropopause and stratosphere, as indicated by the correlation between the longitudinal profiles of 500 hPa temperature and tropopause height and tropopause height and TCO over the latitude range 45–65°S. Spring shows the strongest coupling between tropopause height and TCO in both the model and observational data. In comparison, tropospheric coupling is weaker in ACCESS-CCM and evidently absent in ERA-Interim. For summer, ACCESS-CCM generally shows the opposite behaviour to spring, with diminished stratospheric coupling with the tropopause and dominant tropospheric coupling. In this season, a dominant tropospheric coupling is indicated for ERA-Interim, although the correlation between tropopause height and TCO is higher than for ACCESS-CCM. It is seen that ACCESS-CCM captures the differences in the correlations between seasons reasonably well compared to ERA-Interim. Taken together, these results suggest that the effects of tropospheric variability that act on the height of the tropopause and potentially on the distribution of the stratospheric ozone column can at least be expected to be diminished in spring compared with summer.

Fig. 3 shows the zonal locations of TCO$_{max}$ and TCO$_{min}$ as a function of latitude separately in spring and summer over 1979–2010 for the REF-C1, REF-C2, SEN-C2-fODS and
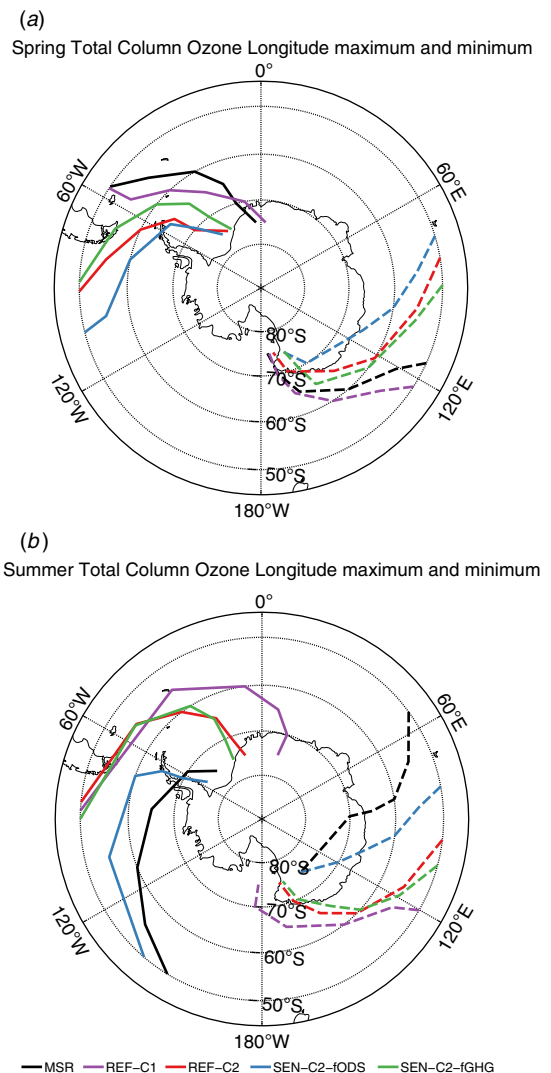

(*a*) Spring Total Column Ozone Longitude maximum and minimum

(*b*) Summer Total Column Ozone Longitude maximum and minimum

Fig. 3. (*a*) Spring and (*b*) summer latitudinal variation of TCO$_{max}$ and TCO$_{min}$ longitude locations averaged over the 1979–2010 period for the MSR dataset and the REF-C1, REF-C2, SEN-C2-fODS and SEN-C2-fGHG simulations. Dashed lines represent the location of TCO$_{max}$, while solid lines represent the location of TCO$_{min}$.

SEN-C2-fGHG simulations and the MSR observational dataset. TCO_{max} and TCO_{min} tend to be located further eastward as latitude increases and are seen to spiral around Antarctica. This eastward shift was reported previously by Grytsai *et al.* (2007*a*, 2007*b*), who suggested that the zonal extremes follow the Antarctic continental boundary, especially near features that have a meridional orientation. In Fig. 3, the TCO_{min} at the lowermost latitudes tends to lie near the Andes, especially during spring. In summer, the MSR and SEN-C2-fODS at the lowermost latitudes are located further west near 140°W. Further south, between 65 and 75°S, the location of TCO_{min} is situated near the Antarctic coastline around the Weddell Sea area between 0 and 60°W. In comparison, the location of the TCO_{max} at 75°S is relatively consistent across the simulations and observations, being situated at the eastern boundary of the Ross Sea, close to 180°E. Even though the well-defined structure during spring is not as apparent during summer, there are similar indications of an influence from the Antarctic topography on the locations of the TCO_{max} and TCO_{min}.

In Fig. 3 it is seen that the phase of the REF-C1 simulation has a closer correspondence with the observations during spring compared to the projection simulations. The only significant differences in the input forcing between the REF-C1 and REF-C2 simulations are that the REF-C1 simulation used observed SSTs and SICs, while for REF-C2, these fields were prescribed by a HadGEMS2-ES simulation. However, there are also large differences between REF-C2 and SEN-C2-fODS during summer, which both have the same prescribed SSTs and SICSs. Therefore, it is unlikely that any differences in SSTs and SICs are producing significant changes. During summer, the zonal structure of the REF-C1 simulation is similar to the projection simulations in showing an eastward shift with increasing latitude. This can also be seen in the MSR data of Fig. 2, where the emergence of a wave-3 component between spring and summer is possibly responsible for shifting the location of TCO_{min} westward, which is not seen for the REF-C2 simulation. This is potentially an effect of the delayed break-up of the ozone hole in the model compared with observations, which was shown to be several weeks later (Stone *et al.* 2016). This may also reduce the influence of the wave-3 component. A delayed break-up of the vortex for other model simulations has also recently been shown by Rao and Garfinkel (2021). In Fig. 3, the SEN-C2-fODS simulation, in which ozone annually varies in a pre-ozone hole prescribed manner, shows a latitudinal variation of TCO_{max} and TCO_{min} that is largely different from REF-C2, especially in summer. Overall, Fig. 3 suggests that ozone depletion plays a noticeable role in controlling the location of the locations of TCO_{max} and TCO_{min}.

Fig. 4 shows the time series of 10-year running-mean spring and summer TCO wave-1 phases at 50°S and 70°S over the period 1979–2010 for MSR, 1960–2010 for REF-C1 and 1960–2100 for REF-C2, SEN-C2-fODS and SEN-C2-fGHG. The phase of the MSR and REF-C1 data are normalised to the phase of REF-C2 so temporal changes can be more easily compared. Regression fits to the projection simulations are also shown for reference. For the historical period, the REF-C1 and REF-C2 time series agree well with MSR during spring and summer at both latitudes, with the exception of spring at 70°S. However,

this is also the latitude location and season that exhibits the smallest temporal phase changes, and it is therefore likely that the differences between REF-C1 and both MSR and REF-C2 are due to the large variability that is seen. In both spring and summer during the period since 2010, it appears that ozone depletion forces an eastward shift in wave-1 phase, while ozone recovery forces a westward shift (as indicated by the behaviour of the SEN-C2-fGHG simulation). Note that, at 70°S, GHG changes appear to produce a clear overall eastward shift in the phase of wave-1 by 2100, which is absent at 50°S.

4 Drivers of zonal wave change

Fig. 5 shows the longitude shift and associated 95% confidence intervals of zonal wave-1 in TCO and 10 hPa zonal wind over the 1960–2000 and 2001–2100 periods for spring and summer from the REF-C2, SEN-C2-fODS and SEN-C2-fGHG simulations at latitudes of 50, 60 and 70°S.

For TCO, the regression model fit shows that both ozone depletion and increasing GHGs over the 1960–2000 period produce an eastward shift in the phase of the zonal wave-1. At 50°S and 60°S, ozone depletion appears to have the largest influence, of up to approximately $38°E \pm 12°$, for SEN-C2-fGHG. However, at 70°S, GHGs appear to have the largest influence, of $25°E \pm 9°$, for SEN-C2-fODS. It is unsurprising to see the largest ozone influence at the lower latitude, where the trends in the polar vortex strength are greatest (Eyring *et al.* 2013*a*). This is not the case for GHGs however, whose impact at 50°S appears minimal. It is likely that at lower latitudes, the influence of GHGs on the phase is hindered by the Andes, which is a large orographic feature that drives the structure of planetary wave formation. At 70°S, the effect of the Andes is diminished, allowing GHGs to have a larger effect. Over the 2001–2100 period, the influence from ozone depletion reverses during the recovery phase, with a near equal and opposite change compared to 1960–2010. Increasing GHGs, on the other hand, continue to force an eastward shift, with a further $32°E \pm 12°$ shift at 70°S shown by the SEN-C2-fODS simulation. This results in GHGs being the major driver at 70°S in spring in the 21st century, resulting in a continued, but diminished, eastward shift in the phase of zonal wave-1. At 50 and 60°S, a westward shift in the zonal wave-1 is suggested by the model, as ozone influences outweigh those of GHGs. However, the westward shift occurs much slower compared to the eastward changes over 1960–2000.

The summer period tells a very similar story. The phase changes are larger and with less variation in TCO. Ozone depletion over the 1960–2000 period produces a change of approximately $60°E \pm 17°$ at 60°S in both the REF-C2 and SEN-C2-fGHG simulations. The influence of ozone depletion at 70°S is also significant compared to spring, with a change of approximately $40°E \pm 19°$. The GHG influence over 1960–2000 is also larger compared to spring at 60 and 70°S, with the most significant change being $34°E \pm 15°$ over 1960–2000 and $44°E \pm 19°$ over 2001–2100 in the SEN-C2-fODS simulation at 70°S. In contrast to spring, the increased influence of ozone at 70°S appears to counteract the GHG effects, which results in a relatively stable zonal wave-1 phase over the 21st century. However, again at 50 and 60°S, a gradual westward shift
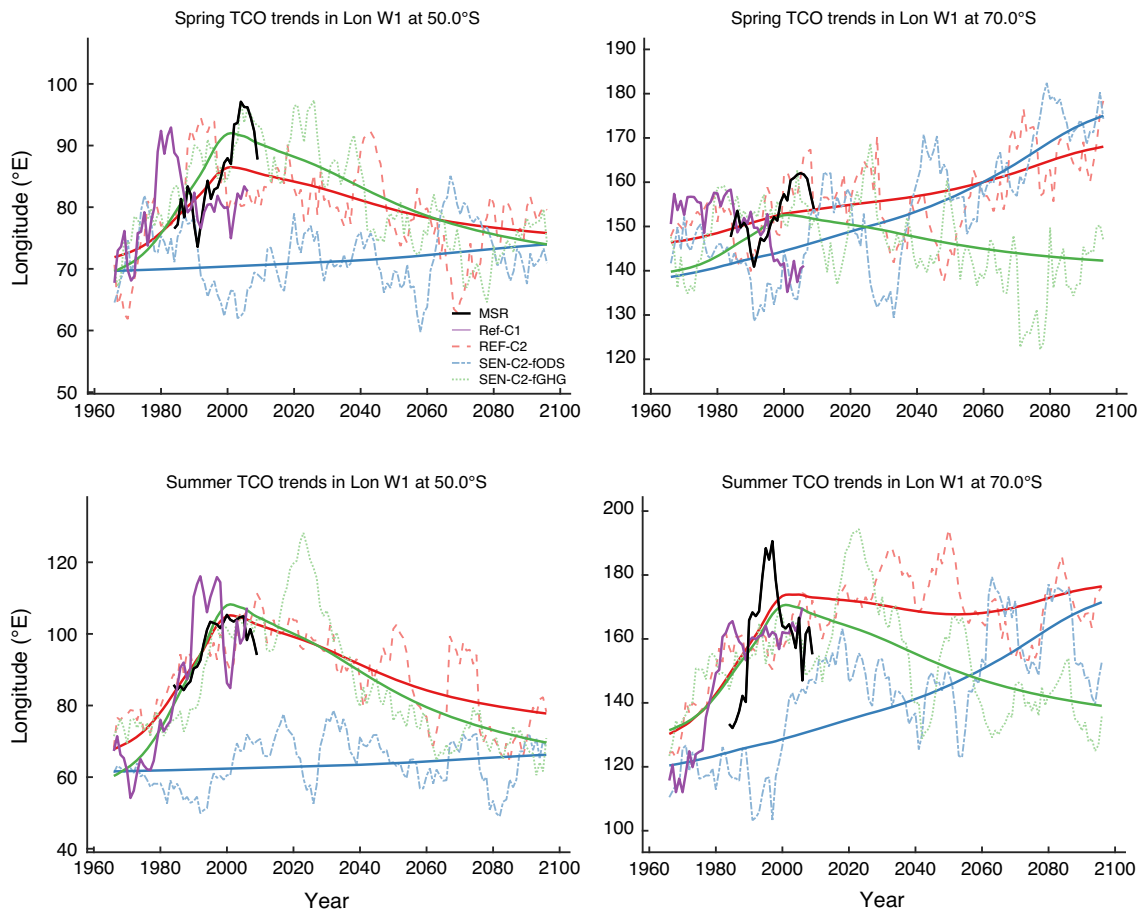
Fig. 4. Seasonal phase changes in the TCO wave-1 component at 50 and 70°S for MSR observations over the 1979–2014 period, compared to the REF-C2, SEN-C2-fODS and SEN-C2-fGHG simulations over the 1960–2100 period. Time series have been produced from a 10-year running mean of the seasonal averages. The MSR and REF-C1 observations have been scaled to the REF-C2 mean between 1979 and 2014. Solid lines show the regression model fits to the data.

occurs as ozone recovery incites a westward phase change of up to 50° compared to an eastward change due to GHGs increases of 25°.

There are some noteworthy differences in the phase of wave-1 in the 10 hPa zonal wind compared with that for TCO. First, at 50°S, GHGs have the largest influence on wave-1 phase, producing a shift of up to approximately $26°E \pm 10°$ over 1960–2000 and $34°E \pm 12°$ over 2001–2100 in the SEN-C2-fODS simulation. There is little significant influence from ozone depletion or recovery. This is interesting, as increasing GHGs have been shown to have little influence on phase changes in TCO at 50°S within our simulations. However, links between the strength of the northern hemisphere subtropical jet, which is influenced greatly by GHG changes, and stratospheric stationary waves at high altitudes has been shown previously (Wang and Kushner 2011). This link is also apparent in the SH, with the strength of the subtropical jet having been shown to shift the phase of wave-1 in stratospheric geopotential heights at 30°S and 10 hPa (Wang *et al.* 2013). The majority of ozone depletion happens lower down, and therefore, TCO phase

changes at lower latitudes will be less influenced by GHGs. Overall, zonal wave-1 at 10 hPa will continue to travel eastward, forced by increasing GHGs.

The eastward change forced by GHGs on 10 hPa zonal wind is also seen during summer during both the 1960–2000 and 2001–2100 periods, however with a larger amount of variation. Again, little to no significant impact is seen due to ozone depletion or recovery. This highlights that the influence of ODS on the phase of wave-1 in TCO is not reproduced in the phase of wave-1 in the 10 hPa zonal wind. This is likely due to ozone changes, and therefore, changes in the strength of the polar vortex are occurring at lower altitudes.

Not only do ODSs and GHGs affect the phase of the zonal wave-1 in TCO, they also have a strong influence on wave amplitude, as shown in Fig. 6. The springtime influence from ozone depletion and recovery on amplitude somewhat replicates the sense of changes that were seen in the phase of wave-1, with depletion (recovery) causing an increase (decrease) in amplitude. However, there is a large amount of interannual variability, with almost no values significant at the 90% confidence interval.
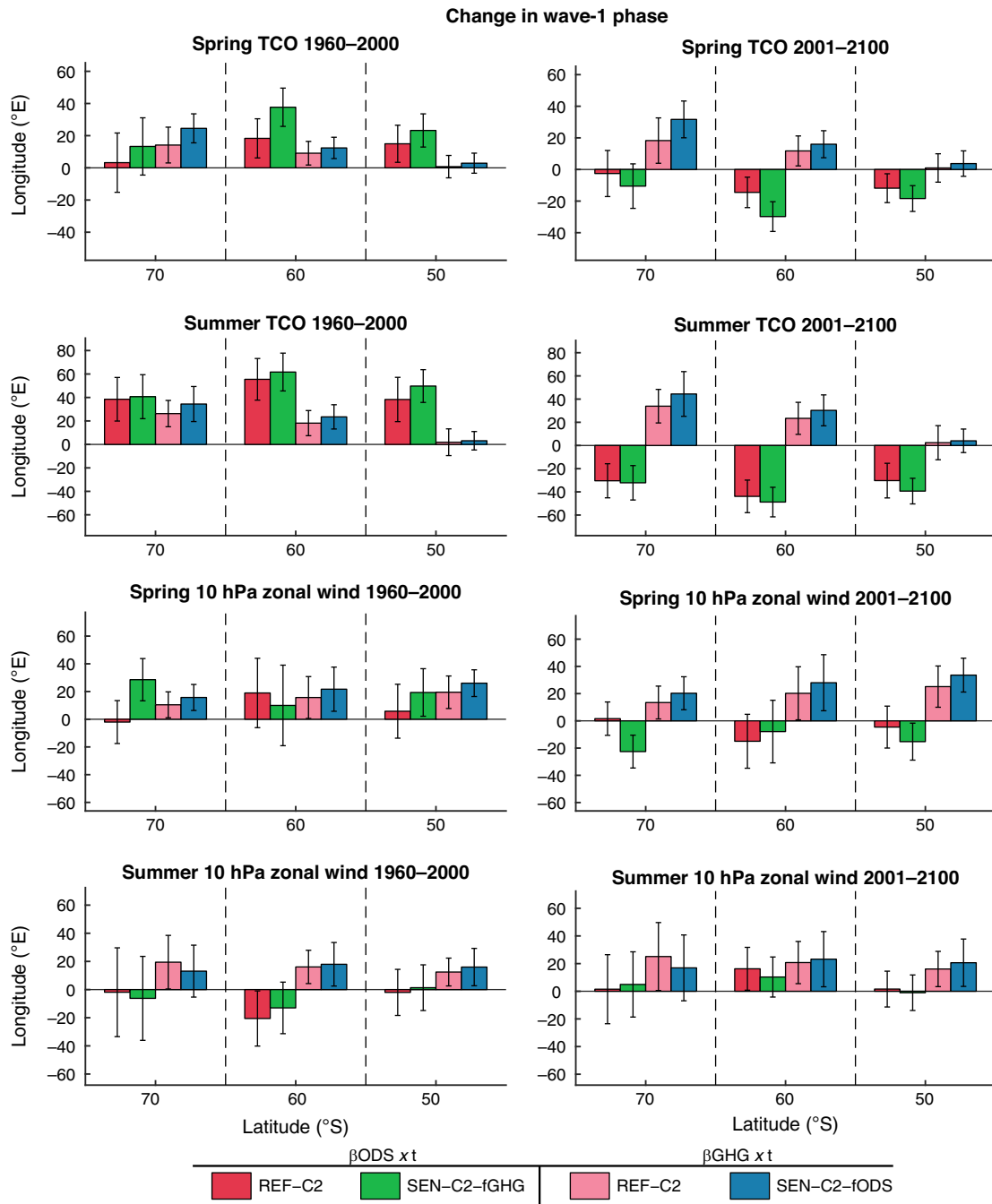
Change in wave-1 phase

Fig. 5.   Changes in the zonal wave-1 regression fits and 95% confidence intervals for spring and summer TCO and 10 hPa zonal wind wave-1 phase over time *t* for 1960–2000 and 2001–2100. The regression fits correspond to Section 3.

The influence from GHGs appears to drive a small decrease in the amplitude of wave-1, most significantly at 60 and 50°S, especially over the 2001–2100 period, where it is on par with the influence from ozone recovery. In similar analysis of temperature at 50 hPa (see Supplementary Fig. S2), GHGs cause a reduction in wave-1 amplitude.

For summer, the amplitude change attributed to both ODSs and GHGs is generally greater than for spring. Ozone depletion

is seen to drive an increase in the TCO zonal wave-1 amplitude by up to 24 ± 4 DU in the SEN-C2-fGHG simulation at 70°S during 1960–2000. This change is approximately halved at 60°S and is not significant at 50°S. The amplitude change due to increasing GHGs is consistently negative over the three latitudes and significantly smaller in magnitude at 60 and 70°S than the change forced by ODS. Over 2001–2100, the TCO wave amplitude is reduced by ozone recovery, with the REF-C2
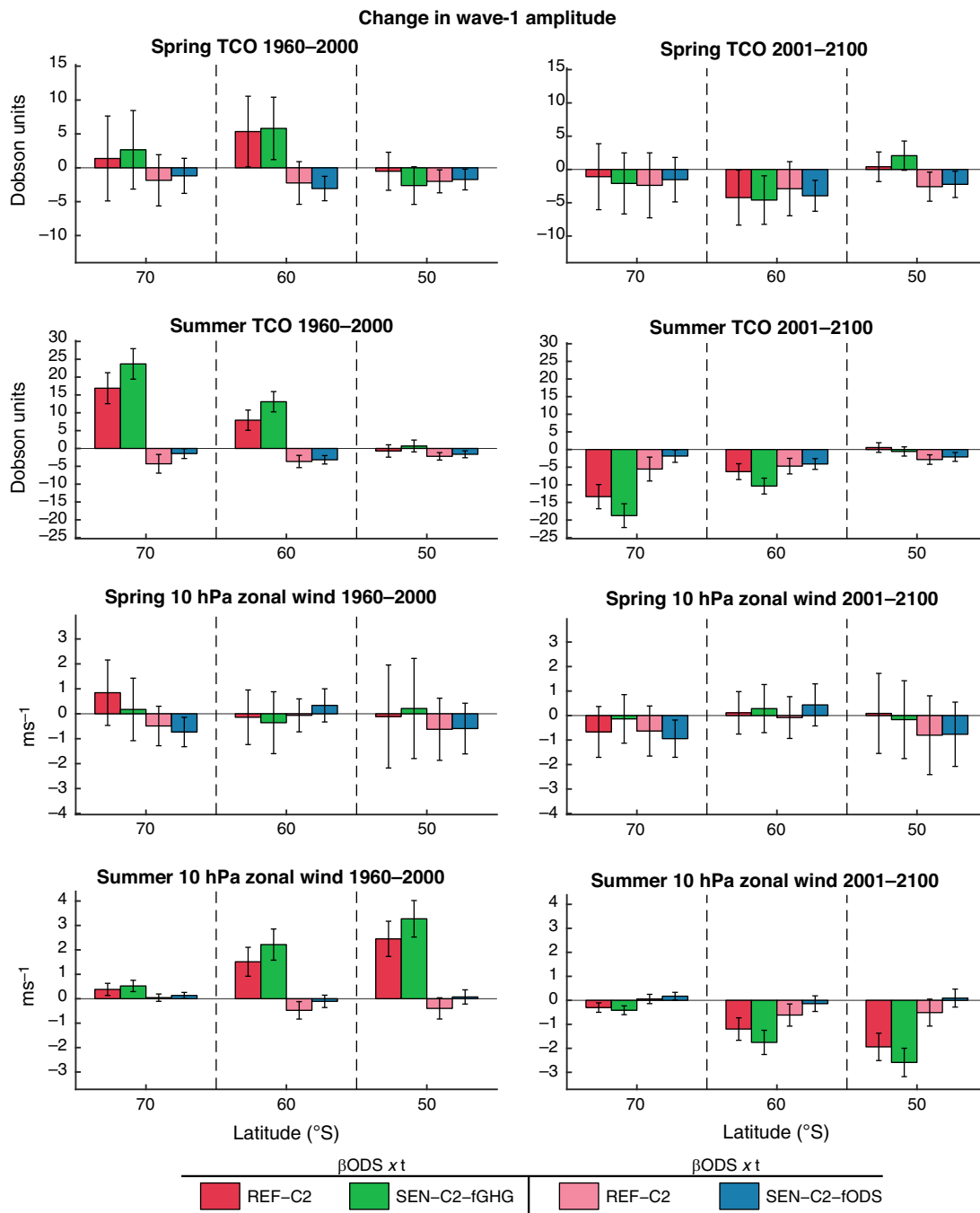
Fig. 6. Same as Fig. 5, but for amplitude.

simulation suggesting that the amplitude at the end of the 21st century will be similar to 1960 levels. These results agree with Wang *et al.* (2013), who suggested that GHGs contributed very little to changes in the amplitude of the wave-1 in stratospheric temperature between October and December.

During spring, the amplitude of wave-1 in the 10 hPa zonal wind shows no significant influence from changes in either ODSs or GHGs. However, during summer, large changes appear

to be driven by ODSs, particularly at 50°S and, to a lesser extent, at 60°S. At 50°S, during 1960–2000, the amplitude increases significantly by $3.2 \pm 0.7\,ms^{-1}$ due to ozone depletion as indicated by the SEN-C2-fGHG simulation. Over the 2001–2100 period, the amplitude changes due to ozone recovery mostly reverse and return to near 1960 levels by the end of the 21st century. It has been shown that large stratospheric planetary wave amplitude changes are followed by similar changes in the
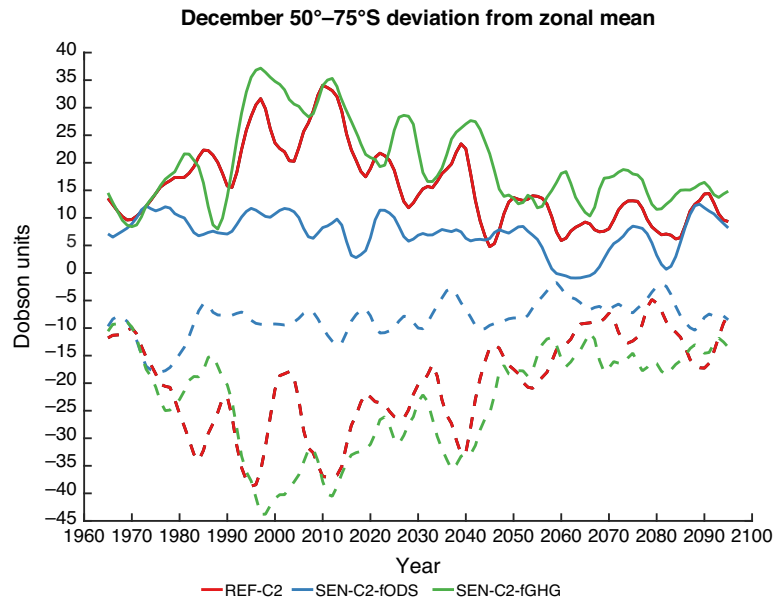
December 50°–75°S deviation from zonal mean

Fig. 7. December TCO deviations from the zonal mean for two longitudes near the TCO_{max} and TCO_{min} locations for each respective simulation (see Fig. 3*b*). For REF-C2 and SEN-C2-fGHG, the solid lines represent the 110°E longitude location and the dashed lines represent the 330°E longitude location. For SEN-C2-fODS, the solid line represents 80°E, and the dashed line represents 300°E.

troposphere (e.g. Thompson *et al.* 2005; Dennison *et al.* 2015). In this way, the large ODS-driven changes in the amplitude of wave-1 in the 10 hPa zonal wind could potentially be an important driver of the tropospheric Southern Annular Mode (SAM) changes that have been observed during late summer and early autumn (WMO 2014). However, the stratospheric polar vortex in the ACCESS-CCM simulations tends to break-down several weeks later than observed (Stone *et al.* 2016), which also occurs in other models (Rao and Garfinkel 2021), and may coincidentally shift the timing of stratospheric variability to overlap with the period of tropospheric SAM trends. It has also been noted that the timing of the final warming in the SH is influenced strongly by ozone depletion and recovery (Wilcox and Charlton-Perez 2013).

Our simulations indicate that increasing GHGs act to decrease the amplitude of wave-1, especially in TCO and 50 hPa temperature. However, this influence is small compared to the amplitude changes due to ozone depletion and recovery. We suspect that the decrease in the amplitude of the wave due to GHG changes is primarily driven from the troposphere. This was investigated by conducting the same analysis on 500 hPa temperature (see Supplementary Figs S1 and S2). It is found that during summer, there is a significant reduction in the 500 hPa wave-1 amplitude at 60 and 70°S that is driven by increasing GHGs. This will likely influence the amplitude of stratospheric QSWs.

5 Impact on localised recovery

A consequence of the phase changes in stratospheric QSWs is that there are potentially significant regional differences in the trends of ozone depletion and recovery along particular zones.

This is shown in Fig. 7, where the deviation from the TCO zonal mean at two different longitudes is shown. The longitudes selected correspond to locations near the TCO_{min} and TCO_{max} in December between 50 and 75°S. Based on Fig. 3*b*, the location at 110°E is slightly eastward of the climatological ozone maximum, while the location at 330°E is slightly eastward of the climatological ozone minimum for REF-C2 and SEN-C2-fGHG. For SEN-C2-fODS, the locations of 80 and 300°E were chosen. The phase shift of wave-1 in TCO leads to significant localised change in ozone concentrations in the REF-C2 and SEN-C2-fGHG simulations. At 110°E, the maximum deviation from the zonal mean is approximately +35 DU. The opposite effect is seen at 330°E, where the deviation is over −40 DU. By contrast, the SEN-C2-fODS simulation shows only small changes on the order of a few DU over the 1960–2100 period. This is likely due to SEN-C2-fODS experiencing no ozone depletion, and therefore, smaller changes in TCO_{min} and TCO_{max} near the edge of the polar vortex as the zonal wave-1 phase trends eastward with increasing GHGs. Consideration of these deviations could be useful for assessing trends in ecosystem modelling of the region. For example, the location of 330°E is near Cape Horn, where the overturning oceanic circulation enhances the abundance of nutrients, and consequently, the biodiversity near the surface. The surface shortwave radiation changes in the region are likely to be higher than for the zonal mean.

6 Conclusions

The amplitude and phase variations of QSWs in TCO and 10 hPa zonal wind were analysed in ACCESS-CCM using a multiple linear regression model with ODS and GHG regression

functions. Four simulations were used in this study: (1) a hindcast simulation from 1960 to 2010, (2) a projection simulation from 1960 to 2100 (REF-C2), (3) a sensitivity simulation from 1960 to 2100 with fixed ODSs at 1960 levels (SEN-C2-fODS) and (4) a sensitivity simulation from 1960 to 2100 with fixed GHGs at 1960 levels (SEN-C2-fGHG).

The ACCESS-CCM model captures the structure of the zonal wave-1 in observed TCO reasonably well in spring and summer compared with observations. However, there is an offset in the phase and amplitude of the zonal wave-1 between ACCESS-CCM and the MSR dataset, with ACCESS-CCM showing a westward bias of around 10° in spring and 50° in summer and a smaller amplitude of up to 20 DU in spring. The historical eastward trend in the phase of the wave-1 seen in the observations in spring and summer is well-captured by ACCESS-CCM. The phase of wave-1 is also seen to be dependent on latitude, with an eastward shift increasing towards higher latitudes. This shift is simulated reasonably well by the model.

At 50°S, the Andes mountain range near 70°W is the dominant orographic feature along the zone; at 70°S the comparatively lower dome of East Antarctica centred near 120°E is the main orographic feature. The Andes has a significant localised effect on tropopause height, and consequently, on the stratospheric ozone column, which forces a well-defined local TCO_{min} near 290°E in spring at 50°S.

The regression model shows that both ozone depletion/recovery and GHG increases have a large influence on changes in the phase and amplitude of wave-1 during spring and summer in ACCESS-CCM, with an eastward shift associated with ozone depletion and increasing GHGs.

During spring, the GHG influences on the phase of wave-1 in TCO are largest at 70°S of up to $25 \pm 9°$E over 1960–2000 and $32°$E $\pm 12°$ in the 21st century. At 50°S, GHG-induced changes are hindered by the orographic influence of the Andes, but are larger further south. The ODS influence is largest at 50 and 60°S, where ozone depletion/recovery has the largest influence on polar vortex strength, outweighing that of GHGs, with an induced change of $38 \pm 12°$E over 1960–2000 at 60°S, which is then effectively reversed during ozone recovery. Contrary to spring, ODSs and GHGs induce phase changes that are generally larger in summer, and the summer phase change at 70°S is influenced nearly equally by GHGs and ODSs. Over 2001–2100, at 70°S, the GHG-induced change of up to $44°$E $\pm 19°$E is largely counteracted by ozone recovery.

These eastward phase trends are generally most significantly influenced by changes in ozone concentration and agree well with previous work by Grytsai *et al.* (2007*b*), who showed an eastward shift in the TCO_{min} of around 45° between 1979 and 2005.

The phase changes in wave-1 for the zonal wind at 10 hPa are driven mainly by GHGs during spring, especially at 50°S. The ODS influence is similar to TCO (a historical eastward shift that is reversed over the 21st century) but is less significant. This is consistent with Wang *et al.* (2013), who showed GHGs influence an eastward phase shift in 10hPa geopotential height, which is linked to changes in the subtropical jet.

Ozone depletion predominantly drives an increase in the amplitude of wave-1 in TCO and 10 hPa zonal wind. This occurs most significantly during summer at 60 and 70°S in TCO and at

50°S in 10 hPa zonal wind. Increasing GHGs, on the other hand, drive a smaller decrease in the amplitude of wave-1 during spring and especially summer, which is in agreement with previous results that suggested that ozone changes were the major driver (Wang *et al.* 2013). During the 21st century, ozone recovery largely reverses the historical amplitude increase, with GHG changes also working to reduce the wave amplitude. In summer, the GHG-influenced reduction in wave amplitude is likely the result of decreased tropospheric wave-1 activity.

Regional changes in the rate of ozone depletion and recovery will accompany variations in the stratospheric zonal asymmetry noted above. Localised deviations in TCO from the zonal mean of up to 40 DU between 50 and 75°S during the ozone hole period are indicated by the model. Over the 21st century, this will result in differing rates of recovery in the ozone column as a function of longitude.

This work shows that changes in ODSs and GHGs have potentially significant influences on the zonal structure of the stratospheric ozone distribution. More robust results from an ensemble of models and simulations is essential for future work.

Conflicts of interest

The authors declare no conflicts of interest.

Declaration of funding

Acknowledgements

References

Brahmananda Rao, V., Fernandez, J. P. R., and Franchito, S. H. (2004). Quasi-stationary waves in the Southern Hemisphere during El Niño and La Niña events. *Ann. Geophys.* **22**, 789–806. doi:10.5194/ANGEO-22–789-2004

Brasseur, G., and Solomon, S. (2005). 'Aeronomy of the middle atmosphere: chemistry and physics of the stratosphere and mesosphere.' (Springer Dordrecht: Netherlands)

Charney, J. G., and Drazin, P. G. (1961). Propagation of planetary-scale disturbances from the lower into the upper atmosphere. *J. Geophys. Res.* **66**, 83–109. doi:10.1029/JZ066I001P00083

Covey, C., Lindzen, R. S., Fasullo, J., and Taylor, K. E. (2020). Quasi-stationary Planetary Scale Waves in Modern Climate Models. United States. doi:10.2172/1716593

Dee, D. P., Uppala, S. M., Simmons, A. J., Berrisford, P., Poli, P., Kobayashi, S., Andrae, U., Balmaseda, M. A., Balsamo, G., Bauer, P., Bechtold, P., Beljaars, A. C. M., van de Berg, L., Bidlot, J., Bormann, N., Delsol, C., Dragani, R., Fuentes, M., Geer, A. J., Haimberger, L., Healy, S. B., Hersbach, H., Hólm, E. V., Isaksen, L., Kållberg, P., Köhler, M., Matricardi, M., Mcnally, A. P., Monge-Sanz, B. M., Morcrette, J. J., Park, B. K., Peubey, C., de Rosnay, P., Tavolato, C., Thépaut, J. N., and sVitart, F. (2011). The ERA-Interim reanalysis: Configuration and

performance of the data assimilation system. *Quart. J. Roy. Meteor. Soc.* **137**, 553–597. doi:10.1002/QJ.828

Dennison, F. W., McDonald, A. J., and Morgenstern, O. (2015). The effect of ozone depletion on the Southern Annular Mode and stratosphere-troposphere coupling. *J. Geophys. Res. Atmos.* **120**, 1–8. doi:10.1002/2014JD023009

Dennison, F., McDonald, A., and Morgenstern, O. (2017). The Evolution of Zonally Asymmetric Austral Ozone in a Chemistry Climate Model. *Atmos. Chem. Phys.* **17**, 14075–14084. doi:10.5194/ACP-2017-405

Evtushevsky, O. M., Grytsai, A. V., Klekociuk, A. R., and Milinevsky, G. P. (2008). Total ozone and tropopause zonal asymmetry during the Antarctic spring. *J. Geophys. Res. Atmos.* **114**, 1–12. doi:10.1029/2008JD009881

Eyring, V., Arblaster, J. M., Cionni, I., Sedláček, J., Perlwitz, J., Young, P. J., Bekki, S., Bergmann, D., Cameron-Smith, P., Collins, W. J., Faluvegi, G., Gottschaldt, K. D., Horowitz, L. W., Kinnison, D. E., Lamarque, J. F., Marsh, D. R., Saint-Martin, D., Shindell, D. T., Sudo, K., Szopa, S., and Watanabe, S. (2013a). Long-term ozone changes and associated climate impacts in CMIP5 simulations. *J. Geophys. Res. Atmos.* **118**, 5029–5060. doi:10.1002/JGRD.50316

Eyring, V., Lamarque, J.-F., Hess, P., Arfeuille, F., Bowman, K., Chipperfield, M. P., Duncan, B., Fiore, A., Gettelman, A., Giorgetta, M. A., Granier, C., Hegglin, M., Kinnison, D., Kunze, M., Langematz, U., Luo, B., Martin, R., Matthes, K., Newman, P. A., Peter, T., Robock, A., Ryerson, T., Saiz-Lopez, A., Salawitch, R., Schultz, M., Shepherd, T. G., Shindell, D., Stähelin, J., Tegtmeier, S., Thomason, L., Tilmes, S., Vernier, J.-P., Waugh, D. W., and Young, P. J. (2013b). Overview of IGAC/SPARC Chemistry-Climate Model Initiative (CCMI) Community Simulations in Support of Upcoming Ozone and Climate Assessments. *SPARC Newsletter* **40**, 48–66. doi:SPARC Newsletter No. 40, p. 48–66, 2013.

Gabriel, A., Körnich, H., Lossow, S., Peters, D. H. W., Urban, J., and Murtagh, D. (2011). Zonal asymmetries in middle atmospheric ozone and water vapour derived from Odin satellite data 2001–2010. *Atmos. Chem. Phys.* **11**, 9865–9885. doi:10.5194/ACP-11-9865-2011

Gerber, E. P. (2012). Stratospheric versus Tropospheric Control of the Strength and Structure of the Brewer–Dobson Circulation. *J. Atmos. Sci.* **69**, 2857–2877. doi:10.1175/JAS-D-11-0341.1

Grytsai, A. V., Evtushevsky, O. M., Agapitov, O. V., Klekociuk, A. R., and Milinevsky, G. P. (2007a). Structure and long-term change in the zonal asymmetry in Antarctic total ozone during spring. *Ann. Geophys.* **25**, 361–374. doi:10.5194/ANGEO-25-361-2007

Grytsai, A. V., Evtushevsky, O. M., Milinevsky, G. P., and Agapitov, O. V. (2007b). Longitudinal position of the quasi-stationary wave extremes over the Antarctic region from the TOMS total ozone. *Int. J. Remote Sens.* **1161**, 37–41. doi:10.1080/01431160600768021

Hartmann, D. L. (1977). Stationary planetary waves in the southern hemisphere. *J. Geophys. Res.* **82**, 4930–4934. doi:10.1029/JC082I031P04930

Hoinka, K. P. (1998). Statistics of the Global Tropopause Pressure. *Mon. Wea. Rev.* **126**, 3303–3325. doi:10.1175/1520-0493(1998)126<3303:SOTGTP>2.0.CO;2

Ialongo, I., Sofieva, V., Kalakoski, N., Tamminen, J., and Kyrölä, E. (2012). Ozone zonal asymmetry and planetary wave characterization during Antarctic spring. *Atmos. Chem. Phys.* **12**, 2603–2614. doi:10.5194/ACP-12-2603-2012

Inatsu, M., and Hoskins, B. J. (2004). The zonal asymmetry of the Southern Hemisphere winter storm track. *J. Climate* **17**, 4882–4892. doi:10.1175/JCLI-3232.1

Karoly, D. J. (1985). An atmospheric climatology of the Southern Hemisphere based on ten years of daily numerical analyses (1972-82): II Standing wave climatology. *Aust. Meteor. Mag.* **33**, 106–116.

Karoly D. J., Vincent D. G. (Eds) (1998). 'Meteorology of the Southern Hemisphere.' (American Meteorological Society: Boston, MA) . doi:10.1007/978-1-935704-10-2

Kurzeja, R. J. (1984). Spatial Variability of Total Ozone at High Latitudes in Winter. *J. Atmos. Sci.* **41**, 695–697. doi:10.1175/1520-0469(1984)041<0695:SVOTOA>2.0.CO;2

Meinshausen, M., Smith, S. J., Calvin, K., Daniel, J. S., Kainuma, M. L. T., Lamarque, J., Matsumoto, K., Montzka, S. A., Raper, S. C. B., Riahi, K., Thomson, A., Velders, G. J. M., and van Vuuren, D. P. P. (2011). The RCP greenhouse gas concentrations and their extensions from 1765 to 2300. *Climatic Change* **109**, 213–241. doi:10.1007/S10584-011-0156-Z

Morgenstern, O., Braesicke, P., O'Connor, F. M., Bushell, A. C., Johnson, C. E., Osprey, S. M., and Pyle, J. A. (2009). Evaluation of the new UKCA climate-composition model – Part 1: The stratosphere. *Geosci. Model Dev.* **2**, 43–57. doi:10.5194/GMD-2-43-2009

Morgenstern, O., Zeng, G., Dean, S. M., Joshi, M., Abraham, N. L., and Osprey, A. (2014). Direct and ozone-mediated forcing of the Southern Annular Mode by greenhouse gases. *Geophys. Res. Lett.* **41**, 9050–9057. doi:10.1002/2014GL062140

Morgenstern, O., Hegglin, M. I., Rozanov, E., O'Connor, F. M., Luke Abraham, N., Akiyoshi, H., Archibald, A. T., Bekki, S., Butchart, N., Chipperfield, M. P., Deushi, M., Dhomse, S. S., Garcia, R. R., Hardiman, S. C., Horowitz, L. W., Jöckel, P., Josse, B., Kinnison, D., Lin, M., Mancini, E., Manyin, M. E., Marchand, M., Marécal, V., Michou, M., Oman, L. D., Pitari, G., Plummer, D. A., Revell, L. E., Saint-Martin, D., Schofield, R., Stenke, A., Stone, K., Sudo, K., Tanaka, T. Y., Tilmes, S., Yamashita, Y., Yoshida, K., and Zeng, G. (2017). Review of the global models used within phase 1 of the Chemistry-Climate Model Initiative (CCMI). *Geosci. Model Dev.* **10**, 639–671. doi:10.5194/gmd-10-639-2017

Newman, P. A., Daniel, J. S., Waugh, D. W., and Nash, E. R. (2007). A new formulation of equivalent effective stratospheric chlorine (EESC). *Atmos. Chem. Phys.* **7**, 4537–4552. doi:10.5194/ACP-7-4537-2007

Niu, X., Frederick, J. E., Stein, M. L., and Tiao, G. C. (1992). Trends in Column Ozone Based on TOMS Data: Dependence on Month, Latitude, and Longitude. *J. Geophys. Res.* **97**, 661–669. doi:10.1029/92JD01392

Quintanar, A. I., and Mechos, C. R. (1995). Quasi-Stationary Waves in the Southern Hemisphere. Part I: Observational Data. *J. Climate* **8**, 2659–2672. doi:10.1175/1520-0442(1995)008<2659:QSWITS>2.0.CO;2

Randel, W. J. (1988). The Seasonal Evolution of Planetary-Waves in the Southern-Hemisphere Stratosphere and Troposphere. *Quart. J. Roy. Meteor. Soc.* **114**, 1385–1409. doi:10.1002/QJ.49711448403

Rao, J., and Ren, R. (2020). Modeling study of the destructive interference between the tropical Indian Ocean and eastern Pacific in their forcing in the southern winter extratropical stratosphere during ENSO. *Climate Dyn.* **54**, 2249–2266. doi:10.1007/S00382-019-05111-6

Rao, J., and Garfinkel, C. I. (2021). Projected changes of stratospheric final warmings in the Northern and Southern Hemispheres by CMIP5/6 models. *Climate Dyn.* **56**, 3353–3371. doi:10.1007/S00382-021-05647-6

Rao, J., Garfinkel, C. I., Chen, H., and White, I. P. (2019). The 2019 New Year Stratospheric Sudden Warming and Its Real-Time Predictions in Multiple S2S Models. *J. Geophys. Res. Atmos.* **124**, 11155–11174. doi:10.1029/2019JD030826

Rayner, N. A., Parker, D. E., Horton, E. B., Folland, C. K., Alexander, L. V., Rowell, D. P., Kent, E. C., and Kaplan, A. (2003). Global analyses of sea surface temperature, sea ice, and night marine air temperature since the late nineteenth century. *J. Geophys. Res.* **108**, 4407. doi:10.1029/2002JD002670

Reichler, T., Dameris, M., and Sausen, R. (2003). Determining the tropopause height from gridded data. *Geophys. Res. Lett.* **30**, 2042. doi:10.1029/2003GL018240

Stone K. A. (2015). Investigating stratospheric ozone change and associated impacts on circulation and climate. PhD Thesis, University of Melbourne. Available at http://hdl.handle.net/11343/91558

Stone, K. A., Morgenstern, O., Karoly, D. J., Klekociuk, A. R., French, W. J., Abraham, N. L., and Schofield, R. (2016). Evaluation of the ACCESS – chemistry–climate model for the Southern Hemisphere. *Atmos. Chem. Phys.* **16**, 2401–2415. doi:10.5194/ACP-16–2401-2016

Thompson, D. W. J., Solomon, S., and Baldwin, M. P. (2005). Stratosphere – Troposphere Coupling in the Southern Hemisphere. *J. Atmos. Sci.* **52**, 708–715. doi:10.1175/JAS-3321.1

Van Der A, R. J., Allaart, M. A. F., and Eskes, H. J. (2015). Extended and refined multi sensor reanalysis of total ozone for the period 1970–2012. *Atmos. Meas. Tech.* **8**, 3021–3035. doi:10.5194/AMT-8–3021-2015

van Loon, H., and Jenne, R. L. (1972). The zonal harmonic standing waves in the southern hemisphere. *J. Geophys. Res.* **77**, 992–1003. doi:10.1029/JC077I006P00992

Varotsos, C., Cartalis, C., Vlamakis, A., Tzanis, C., and Keramitsoglou, I. (2004). The long-term coupling between column ozone and tropopause properties. *J. Climate* **17**, 3843–3854. doi:10.1175/1520-0442(2004)017<3843:TLCBCO>2.0.CO;2

Wang, L., and Kushner, P. J. (2011). Diagnosing the stratosphere-troposphere stationary wave response to climate change in a general circulation model. *J. Geophys. Res. Atmos.* **116**, 1–16. doi:10.1029/2010JD015473

Wang, L., Kushner, P. J., and Waugh, D. W. (2013). Southern hemisphere stationary wave response to changes of ozone and greenhouse gases. *J. Climate* **26**, 10205–10217. doi:10.1175/JCLI-D-13–00160.1

Wilcox, L. J., and Charlton-Perez, A. J. (2013). Final warming of the Southern Hemisphere polar vortex in high- and low-top CMIP5 models. *J. Geophys. Res. Atmos.* **118**, 2535–2546. doi:10.1002/JGRD.50254

Wirth, V. (1993). Quasi-stationary planetary waves in total ozone and their correlation with lower stratospheric temperature. *J. Geophys. Res.* **98**, 8873–8882. doi:10.1029/92JD02820

WMO (2011). Scientific Assessment of Ozone Depletion: 2010. *Global Ozone Research and Monitoring Project–Report No 52* 516.

WMO (2014). Scientific Assessment of Ozone Depletion: 2014. *Global Ozone Research and Monitoring Project–Report No 55* 516.